International Journal of Heat and Mass Transfer 257 (2026) 128217

Contents lists available at ScienceDirect

International Journal of Heat and Mass Transfer

journal homepage: www.elsevier.com/locate/hmt

Experimental and numerical evaluation of convective heat transfer correlations in a packed bed of iron ore pellets

Örjan Fjällborg [a,b,*], Charlotte Andersson [b], Daniel Marjavaara [a], T.K. Sandeep Kumar [c], Anders Dahlin [d]

[a] Luossavaara-Kiirunavaara AB (LKAB), R&D, Kiirunavaaravägen 1, SE-981 86, Kiruna, Sweden
[b] Luleå University of Technology, Div. of Minerals and Metallurgical Engineering (MiMeR), SE-971 87, Luleå, Sweden
[c] Luossavaara-Kiirunavaara AB (LKAB), R&D, Box 952, SE-971 28, Luleå, Sweden
[d] Alteco System AB, Kvarngatan 2, SE-982 32, Gällivare, Sweden

ABSTRACT

Modeling heat transfer in packed bed processes such as iron ore pelletization is essential for optimizing process operation and furnace design. In these systems, materials like magnetite iron ore undergo thermal and chemical transformations, where heat and mass transfer are often coupled with heat effects from multiple processes — including both exothermic chemical reactions (e.g., oxidation) and endothermic physical changes (e.g., drying and sintering). As the industry moves towards fossil-free ironmaking, it becomes increasingly important to isolate pure heat transfer behavior, independent of chemical reactions, to support the development of sustainable process schemes.

This study investigates convective heat transfer in a packed bed by evaluating several established correlations against the conventionally used modified Ranz–Marshall correlation. Pilot pot-scale experiments were performed by isothermally heating 120 kg of already indurated iron ore pellets at 300 °C to avoid chemical reactions, with additional experiments at 500 °C and 700 °C to assess performance at elevated temperatures typical of industrial pelletization.

Results show that the modified Ranz–Marshall correlation underpredicts heat transfer rates under conditions isolating convective heat transfer, reinforcing the need for this investigation. The Wakao–Funazkri and Rowe–Claxton correlations provided the best agreement with experimental data, particularly at 300 °C. Minor deviations at higher temperatures suggest the influence of unaccounted variables, warranting further study. Sensitivity analysis identified gas velocity as the most significant parameter affecting heat transfer. The results suggest that adopting the Wakao–Funazkri and Rowe–Claxton correlations can provide a stronger basis for predictive pellet heat transfer modeling in future process design and simulation work.

1. Introduction

Iron oxide pellets are a critical feedstock in ironmaking, and their importance is expected to grow as the industry transitions to fossil-free technologies such as HYBRIT [1], Midrex-H_2 [2], and others [3–6] to mitigate CO_2 emissions. Their uniform size and spherical shape enhance reactor performance by improving bed permeability, gas flow, and heat distribution, leading to better pellet quality and more efficient process control. During induration, magnetite pellets undergo drying, calcination, and oxidation, with drying and calcination being endothermic and oxidation being highly exothermic, significantly impacting the heat transfer and overall energy balance of the reactor system. The shift to hydrogen-based ironmaking presents opportunities to enrich the pelletizing atmosphere with excess oxygen, thereby accelerating reaction rates — particularly oxidation — and influencing the physical, chemical, and thermal dynamics of the reactor. In this context, process modeling becomes essential for optimizing both existing and future induration processes as well as reactor design. CFD simulations with detailed heat transfer modeling can accurately capture flow and thermal behavior. As a first step, isolating and understanding heat transfer independently from chemical reactions is crucial for developing sustainable and energy-efficient pelletization systems.

In gas–solid systems, heat transfer occurs through convection, conduction, and radiation [7], with convection typically being the dominant mechanism. The convective heat flow rate, $\dot{q}$, can be described by Newton's Law of Cooling [8] as $\dot{q} = h_{tc} A_{srfc} (T_g - T_{srfc})$, where h_{tc} is the convective heat transfer coefficient. Convective heat transfer is commonly characterized by the Nusselt number, $\mathrm{Nu} = h_{tc} L / k_g$, which represents the ratio of convection to conduction at a surface. Empirical correlations typically express Nu as a function of the Reynolds and Prandtl numbers, $\mathrm{Nu} = f(\mathrm{Re}, \mathrm{Pr})$, thereby providing a means to estimate h_{tc} and, in turn, the heat flow rate and surface temperature. While these correlations are well established for idealized particle arrangements, their validity under high-temperature, reactive, or industrially relevant packed-bed conditions remains uncertain.

Convective heat transfer modeling in packed beds of iron ore pellets has been studied, although most existing research focuses on

* Corresponding author at: Luossavaara-Kiirunavaara AB (LKAB), R&D, Kiirunavaaravägen 1, SE-981 86, Kiruna, Sweden.
E-mail address: orjan.fjallborg@lkab.com (Ö. Fjällborg).

https://doi.org/10.1016/j.ijheatmasstransfer.2025.128217
Received 13 August 2025; Received in revised form 25 October 2025; Accepted 1 December 2025
Available online 8 December 2025

Nomenclature

Acronyms

CFD	Computational Fluid Dynamics
LPT	Lagrangian Particle Tracking

Definitions

Particle	A solid that contains porosity
Pellet	Same as particle

English

$\mathbf{D}$	Darcy's coefficient $(1/m^2)$
$\mathbf{F}$	Forchheimer's coefficient $(1/m)$
$\mathbf{q}$	Heat flux vector $(J/(m^2 \cdot s))$
$\mathbf{U}$	Velocity $(m\,s^{-1})$
Δt_e	Effective time-step (s)
$\dot{Q}$	Heat rate of change from chemical reactions $(J/(s \cdot m^3))$
$\dot{q}$	Heat flow $(J\,s^{-1})$
$\dot{q}_{Rtot}$	Total radiative heat flow $(J\,s^{-1})$
$\dot{q}_R$	Emitted radiative heat flow $(J\,s^{-1})$
$\dot{q}_r$	Chemical reaction heat flow $(J\,s^{-1})$
Conv	Asymptotic range of convergence
GCI	Grid convergence index
A	Area (m^2)
A_{pore}	Pore surface area (m^2)
C_p	Specific heat capacity $(J/(kg \cdot K))$
d	Diameter (m)
e	Internal energy $(J\,kg^{-1})$
G	Radiative heat transfer flux $(J/(m^2 \cdot s))$
h	Enthalpy $(J\,kg^{-1})$
h_{tc}	Heat transfer coefficient $(J/(m^2 \cdot s \cdot K))$
K	Kinetic energy $(J\,kg^{-1})$
k	Thermal conductivity $(J/(m \cdot s \cdot K))$
L	Characteristic length (m)
q	Heat flux $(J/(m^2 \cdot s))$
S_{hR}	Energy rate of change source term due to radiation $(J/(m^3 \cdot s))$
S_h	Enthalpy rate of change source term $(J/(m^3 \cdot s))$
S_m	Momentum equation source term (N/m^3)
T	Temperature (K)
t	Time (s)
U	Linear velocity $(m\,s^{-1})$
V	Volume (m^3)

Greek

α_{eff}	Sum of laminar and turbulent thermal diffusivities $(kg/(m \cdot s))$
$\boldsymbol{\tau}$	Viscous momentum flux (J/m^3)
ϵ	Emissivity of the surface (ranges from 0 to 1)
ϵ_b	Void fraction in bed or bed porosity
ϵ_p	Porosity of a particle
κ	Thermal diffusivity (m^2/s)
μ	Fluid dynamic viscosity $(kg/(m \cdot s))$
ν	Fluid kinematic viscosity (m^2/s)
ϕ	Solution variable (K)
ρ	Fluid density (kg/m^3)
σ	Stefan–Boltzmann constant $(5.67037 \times 10^{-8}\ W/(m^2 \cdot K^4))$
ξ	Error estimate

Superscripts

n	current time step
n+1	next time step

Subscripts

p	pressure
0	bulk
1	fine mesh
12	fine relative medium mesh
2	medium mesh
23	medium relative coarse mesh
3	coarse mesh
a	absolute
b	bed
E	environment
e	effective
exact	exact solution
f	fluid
g	gas
p	particle
pz	particle with zero porosity
R	radiation
r	reaction
s	sensible
s	solid
srfc	surface
std	standard

Other Symbols

Bi	Biot number
Nu	Nusselt number
Pr	Prandtl number
Re	Reynolds number
Sc	Schmidt number
Sh	Sherwood number

reacting systems rather than isolating heat transfer effects. Seshadri and Pereira [9], for example, examined convective heat transfer in a packed bed of green pellets, but their study included drying effects, which influence both heat and mass transfer behavior, introducing uncertainty in the contribution of convective heat transfer. Subsequent studies, including Barati [10], have built upon this work, with the modified Ranz–Marshall model frequently adopted due to its widespread use [11–15], among others. However, because the original study focused on reacting systems without isolating convective heat transfer, its applicability remains uncertain. Existing studies often do not isolate convective heat transfer from other factors, such as reaction and drying effects, which introduces uncertainty in the actual contribution of convection. In some cases, deviations in heat transfer and reaction rate calculations may cancel each other out, resulting in seemingly good agreement with experimental data while masking underlying model inaccuracies. Additionally, temperature-dependent specific heat capacity (C_p) is not always reported, even though it can significantly impact the accuracy of thermal simulations. While several empirical correlations are available, their predictive capabilities under non-reacting conditions for packed beds of iron ore pellets have not been thoroughly

Table 1
Summary of correlations for different flow regimes in packed beds of spheres. The Reynolds number (Re) is based on the superficial velocity and the particle diameter as the characteristic length.

Flow condition	Correlation	Eq. no	Name of correlation	Applicability/Notes
Reynolds number up to 2×10^3	$Nu = A + B\,Re^n\,Pr^{2/3}$, $A = \frac{2}{1-\left(1-\epsilon_b\right)^{1/3}}$, $B = \frac{2}{3\epsilon_b}$, $\frac{2-3n}{3n-1} = 4.65\,Re^{-0.28}$	(1)	Rowe and Claxton [16]	Covers porosities $0.260 < \epsilon_b < 0.476$. Validated in cubic and rhombohedral arrays with a heated copper sphere surrounded by table-tennis balls. This setup gives almost no heat conduction between particles and between particles and the walls.
Low to moderate Reynolds number between 15 and 8.5×10^3	$Nu = 2 + 1.1\,Re^{0.6}\,Pr^{1/3}$	(2)	Wakao and Funazkri Correlation [17]	Derived from a meta-analysis of experimental data on heat transfer in packed beds with various particle shapes (spherical and cylindrical), this correlation assumes a typical bed void fraction of $\epsilon_b \approx 0.4$. For cases with high velocity gradients, axial thermal dispersion coefficients should also be applied.
Reynolds Number up to 10^5 (Fully Turbulent)	$Nu = \left(7 - 10\,\epsilon_b + 5\,\epsilon_b^2\right)\left(1 + 0.7\,Re^{1/5}Pr^{1/3}\right) + \left(1.33 - 2.4\,\epsilon_b + 1.2\,\epsilon_b^2\right)Re^{0.7}\,Pr^{1/3}$	(3)	Gunn's Correlation [18]	Used for low to high Reynolds numbers. Also covers moderate to high porosity beds, $0.35 < \epsilon_b < 1.0$.
Reynolds Number up to 10^2	$Nu = \left(7-10\,\epsilon_b+5\,\epsilon_b^2\right)\left(1+0.1\,Re^{1/5}Pr^{1/3}\right) + \left(1.33 - 2.19\,\epsilon_b + 1.15\,\epsilon_b^2\right)Re^{0.7}\,Pr^{1/3}$	(4)	Tavassoli [20]	Tavassoli re-fitted Gunn's correlation using DNS. Applicable for low Reynolds numbers. Also covers moderate porosity beds, $0.35 < \epsilon_b < 1.0$.
Low to high Reynolds number	$Nu_l = 0.664\,Pr^{1/3}\left(\frac{Re}{\epsilon_b}\right)^{1/2}$, $Nu_t = \frac{0.037\left(\frac{Re}{\epsilon_b}\right)^{0.8}Pr}{1+2.443\left(\frac{Re}{\epsilon_b}\right)^{-0.1}\left(Pr^{2/3}-1\right)}$, $Nu_{sp} = 2 + \left(Nu_l^2 + Nu_t^2\right)^{1/2}$, $f(\epsilon_b) = 1 + 1.5\left(1-\epsilon_b\right)$, $Nu = f(\epsilon_b)\,Nu_{sp}$	(5)	Gnielinski [19]	Covers porosities $0.26 < \epsilon_b < 0.935$. Asymptotic solutions for a laminar and a turbulent quantity is combined. This model was used by Achenbach [21] with a single heated copper sphere in an unheated bed of spheres with low conduction through contact points.
Laminar to transitional flow up to $Re \approx 200$	$Nu = 2.0 + 0.6\left(\frac{Re}{\epsilon_b}\right)^{1/2}Pr^{1/3}$	(6)	Modified Ranz–Marshall [11]	A practical adjustment inferred from the original Ranz–Marshall correlation to account for porosity effects in packed beds, with void fractions typically ranging from 0.3 to 0.5.

compared, especially under well-defined conditions, such as isothermal gas temperatures.

This study aims to isolate convective heat transfer from reaction and drying effects by using pre-fired iron ore pellets for experimental validation at isothermal gas temperatures of 300 °C, 500 °C, and 700 °C. The sensitivity of convective heat transfer to variations in gas velocity, particle size, and bed porosity will be analyzed, along with the impact of using a temperature-dependent specific heat capacity (C_p) versus a constant value. Multiple empirical correlations, including those by Rowe and Claxton [16], Wakao and Funazkri [17], Gunn [18], and Gnielinski [19], as well as a more recent correlation by Tavassoli et al. [20], are evaluated to determine their predictive capabilities under non-reacting conditions, as summarized in Table 1. Tavassoli's correlation, derived from high-resolution Direct Numerical Simulations (DNS), provides new insights into heat transfer mechanisms in packed beds and suggests that monodisperse correlations can be used with an effective diameter for accurate predictions in bidisperse packed beds. The Wakao and Funazkri correlation, derived from experimental data corrected for axial thermal dispersion, is widely used due to its broad applicability across various packed bed configurations. Similarly, the Gunn correlation, which incorporates bed porosity effects, covers a broad range of Reynolds numbers and applies to both heat and mass transfer in packed and fluidized beds. The Gnielinski correlation, designed for medium to high Peclet numbers, accounts for both flow and thermal dispersion effects, improving prediction accuracy and bridging the transition between laminar and turbulent regimes.

2. Methodology

This section describes the conditions for the heat transfer experiments in the Pilot Pot Furnace, and how the simulation case was setup and validated in OpenFOAM® .

2.1. Experimental setup

Fig. 1 shows a schematic diagram of the pilot pot furnace, indicating the direction of gas flows and the locations of gas and temperature measurements. Type S thermocouples (accuracy ±1.5 °C, response time 1–2 s without the sheath) were used for temperature measurements within the bed. Fig. 2 shows a thermocouple positioned in the bed before being covered by pellets. The thermocouples were horizontally aligned with an angular spread of approximately 12°. To conduct the heat transfer studies, experiments were performed using 120 kg of fired pellets consisting of approximately 93 % Fe_2O_3. For model validations, a downdraft gas mass flow rate of 700 kg h^{-1} was applied at three different temperatures: 300 °C, 500 °C, and 700 °C, corresponding to gas velocities of approximately 3.15 m s^{-1}, 4.2 m s^{-1}, and 5.2 m s^{-1}, respectively. The heating profile is shown in Fig. 3. After propane combustion and prior to entering the bed, the gas composition was as listed in Table 2. It is important to note that pellet and bed properties remain the same throughout the series of experiments.

Table 3 lists the relevant pellet properties. All values are measured except for the initial pellet heat capacity C_p, which was obtained from the HSC Chemistry database. And Table 4 lists the relevant properties for the porous pellet bed.

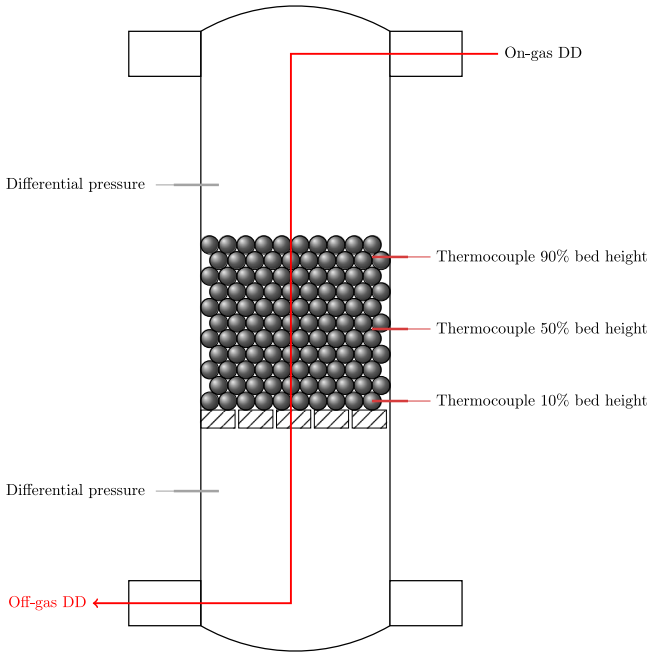

Fig. 1. Schematic diagram of the pilot pot furnace. The oxygen concentration, temperature and mass flow of the process gas before the bed is used to regulate the conditions in the pilot pot furnace. Mass flows of the gas components are measured before combustion, making it possible to calculate the gas composition before the bed, shown in Table 2. DD is downdraft flow.

Fig. 2. Thermocouple measuring temperature approximately 5 cm inside the bed. Image reproduced with permission from Anna Eriksson [22].

Table 2
Gas composition after combustion.

T_g (°C)	N_2 (%)	O_2 (%)	H_2O (%)	CO_2 (%)	Ar (%)
300	76.8	18.3	2.6	1.4	0.9
500	76.3	16.6	3.8	2.4	0.9
700	75.9	14.9	5.0	3.3	0.9

2.2. Numerical model

In this study, modeling and simulation were done using OpenFOAM® v2112, and the Lagrangian particle tracking (LPT) approach, implemented in the solver *reactingHeterogeneousParcelFoam*.

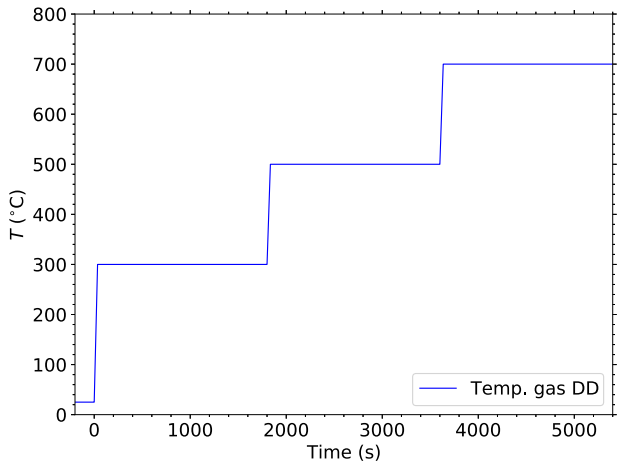

Fig. 3. Heating profile showing the temperature of the down-draft gas above the packed bed.

Table 3
Pellet properties.

Symbol	Value	Description
ϵ_p	0.2146	Pellet porosity[a]
ρ_{pz}	5060 kg/m^3	True (material) density, i.e. pellet with no pores[b]
ρ_p	3974 kg/m^3	Pellet density[c]
T_p	30 °C	Initial temperature[d]
C_p	650 J/(kg K)	Initial heat capacity[b]
d_p	0.012 05 m	Pellet diameter[e]

[a] Measured by pycnometry.
[b] Literature data.
[c] $(1-\epsilon_p)\rho_{pz}$.
[d] Mean of thermocouple measurements in the bed.
[e] Measured data based on two 2D image analyses of pellet size distribution: (1) D_{10} = 11.1 mm, D_{50} = 11.8 mm, D_{90} = 12.8 mm; (2) D_{10} = 11.5 mm, D_{50} = 12.3 mm, D_{90} = 13.1 mm. The mean D_{50} (12.05 mm) was used in the simulations.

Table 4
Bed properties.

Symbol	Value	Description
A_b	0.1 m^2	Bed area
H_b	0.508 m	Bed height
V_b	0.0508 m^3	Bed volume[a]
m_{tot}	120 kg	Total mass
ϵ_b	0.4056	Bed porosity[b]

[a] $A_b \times H_b$.
[b] $1 - \frac{m_{tot}}{V_b \cdot \rho_{pz}(1-\epsilon_p)}$.

Given this solver, it becomes natural to represent the packed bed of iron ore pellets as Lagrangian particles. Although the physical system is a packed bed, the particles are treated as dispersed entities in the simulation for computational efficiency. In this section, the term *particle* is used instead of *pellet* to keep the description more general and applicable beyond iron ore pellet systems.

In this scenario, an energy balance is applied that accounts for the transient changes in the internal energy of the particle, along with the convective heat transfer. Radiative heat transfer is assumed to be small, especially within the packed bed where pellet temperatures are similar, and any heat associated with chemical reactions is assumed negligible since fired pellets was used. When the Biot number is below 0.2 [23,24], internal particle conduction becomes negligible. Table 5 presents estimated Biot numbers for hematite pellets under different gas temperatures. Consequently, the temperature inside the particle is

Table 5
Estimated Biot numbers for iron ore pellets (porosity 0.21, diameter $d_p = 12$ mm)

Gas temp T_g (°C)	Gas conductivity [25] k_g (J/(m s K))	Biot number[a] Bi
300	0.044	4.1×10^{-4}
500	0.056	5.2×10^{-4}
700	0.066	6.1×10^{-4}

[a] Calculated as $Bi = \frac{k_g d_p}{k_p}$, assuming $k_p \approx 1.3$ J/(m s K) for hematite pellets [26].

assumed to be the same as the surface temperature, and T_p is used instead of T_{srfc} in

$$mC_p \frac{dT_p}{dt} = \underbrace{h_{tc} A_{srfc}(T_g - T_p)}_{\dot{q}}. \tag{7}$$

In Eq. (7), m is the particle mass, C_p is its specific heat capacity, and T_p denotes the uniform particle temperature, tracked individually for each particle in the Lagrangian framework. The right-hand side represents convective heat transfer from the gas at temperature T_g to the particle surface, with h_{tc} as the heat transfer coefficient and A_{srfc} as the surface area. The energy balance equation, Eq. (7), is solved analytically for each time step by using the *analytical* integration scheme in OpenFOAM® , yielding an updated temperature for each particle. The gas-phase temperature T_g is obtained from the Eulerian energy equation solved on the computational grid, where source terms account for convective heat exchange with the particles. Since the particle and gas temperatures are solved separately ($T_p \neq T_g$), the model inherently follows a local thermal non-equilibrium (LTNE) formulation. This coupling defines the temperature development for both solid and fluid phases.

The governing equations for mass, momentum, and energy describe the continuous phase, while source and sink terms model the interactions with the particles. Together, the particles form a packed bed, whose thermal effect is captured via a volumetric heat source term, while the flow resistance is modeled as a momentum sink term. All variables are defined in the Nomenclature section.

The mass conservation equation for a compressible flow is:

$$\frac{\partial \rho}{\partial t} + \nabla \cdot (\rho \mathbf{U}) = 0. \tag{8}$$

The momentum equation is modified by a sink term representing the resistance caused by the packed bed of iron ore pellets. For a laminar compressible Newtonian fluid, it is given by [27]:

$$\frac{\partial \rho \mathbf{U}}{\partial t} + \nabla \cdot (\rho \mathbf{U}\mathbf{U}) = -\nabla p + \nabla \cdot \boldsymbol{\tau} + S_m, \tag{9}$$

where the viscous stress tensor $\boldsymbol{\tau}$ is defined as

$$\boldsymbol{\tau} = \rho \nu \left(\nabla \mathbf{U} + (\nabla \mathbf{U})^T - \frac{2}{3}(\nabla \cdot \mathbf{U})\mathbf{I} \right), \tag{10}$$

and the momentum sink term S_m is modeled using the Darcy–Forchheimer law, which captures both viscous, inertial, and turbulence effects within the bed. The applied coefficients are derived from the Ergun equation, as detailed in Appendix A. The specific coefficients used in the simulations are provided in Table 6.

The energy equation for the specific enthalpy h includes a source term S_h to account for heat transfer between the continuous phase and the particles:

$$\frac{\partial \rho h}{\partial t} + \nabla \cdot (\rho \mathbf{U} h) - \frac{\partial p}{\partial t} = - \nabla \cdot \mathbf{q} + \nabla \cdot (\boldsymbol{\tau} \cdot \mathbf{U}) + \rho(\mathbf{g} \cdot \mathbf{U}) + S_h. \tag{11}$$

The heat flux is modeled as $\mathbf{q} = -\alpha_{eff} \nabla h$, where α_{eff} is the effective thermal diffusivity of the continuous phase, and ∇h is the spatial gradient of specific enthalpy.

The source term S_h is computed from the right-hand side of Eq. (7), converted to a volumetric form:

$$S_h = \frac{\dot{q}}{V_p}. \tag{12}$$

2.2.1. Modeling assumptions

The following assumptions are made in the modeling of heat transfer in the iron ore pellet bed within the Pilot Pot Furnace:

1. **Spatial dimensions:** The system is assumed to be one-dimensional. This simplification is motivated by the geometric symmetry and dominant heat transfer direction.
2. **Flow regime:** While Reynolds numbers in the bed reach 568–825, the momentum sink term is modeled using the Darcy–Forchheimer law with coefficients fitted to experimental pressure drop. This approach captures viscous, inertial, and early turbulence effects [28] without requiring an explicit turbulence model in the porous medium. For the bulk gas flow outside the bed, laminar flow is assumed, as Reynolds numbers remain below 1000.
3. **Chemical composition:** The bed is assumed to consist entirely of hematite (Fe_2O_3). Minor components such as other metal oxides are neglected, as their impact on bulk heat capacity is considered negligible in this context.

2.2.2. Model setup

The following model setup choices were made for the heat transfer simulations:

1. **Time scale:** A transient formulation is used, with the second-order accurate Crank–Nicholson scheme applied to all time-derivative terms due to its robustness, accuracy, and suitability for unsteady problems [29].
2. **Spatial discretization — divergence terms:** The `linearUpwind` scheme is selected for all divergence terms to maintain second-order accuracy while minimizing numerical diffusion.
3. **Dynamic viscosity:** Temperature-dependent viscosity is modeled using Sutherland's law [30]:
$$\mu = \mu_{ref} \left(\frac{T}{T_{ref}} \right)^{3/2} \frac{T_{ref} + S}{T + S} \tag{13}$$
where T_{ref} is a reference temperature, μ_{ref} is the dynamic viscosity at T_{ref}, and S is the Sutherland temperature.
4. **Equation of state and thermodynamics:** The gas phase is modeled as an ideal gas, where the density ρ is related to pressure p, temperature T, and the specific gas constant R according to the ideal gas law:
$$\rho = \frac{p}{RT}. \tag{14}$$
This couples pressure and velocity with the gas density field. The gas density also satisfies the mass conservation equation:
$$\frac{\partial \rho}{\partial t} + \nabla \cdot (\rho \mathbf{U}) = S_\rho \tag{15}$$
where S_ρ is a mass source term due to the Lagrangian bed particles. The gas-phase momentum and mass equations are solved alternately to ensure convergence.
5. **Gas-phase heat conduction:** The Laplacian term is discretized using the second-order accurate `linear` interpolation scheme.
6. **Thermodynamic data:** Temperature-dependent thermodynamic properties for gas species (e.g., heat capacity and enthalpy) are obtained from JANAF thermochemical tables.

Table 6
Darcy–Forchheimer parameters.

Symbol	Value	Description
D	5.47E6	Darcy parameter
F	2.587E3	Forchheimer parameter

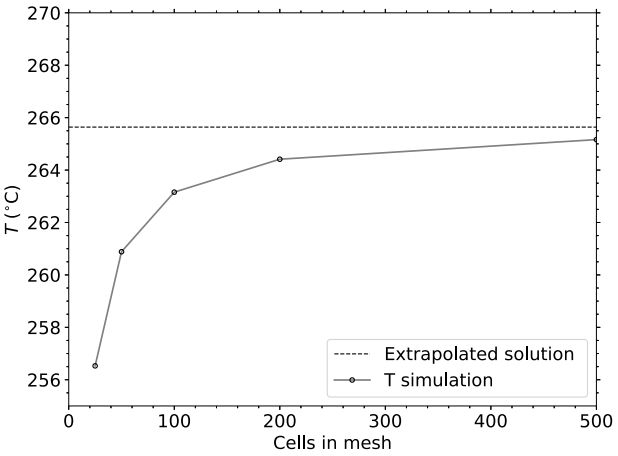

Fig. 4. Mesh independence study for different mesh fineness, with Richardson's extrapolation (Eq. (B.2)). The solution variable is the particle temperature at a bed depth of 0.25 m and time 400 s.

2.3. Sensitivity analysis

To investigate the impact of minor variations in boundary conditions on heat transfer to the bed, a sensitivity analysis was conducted on selected variables that were believed to significantly influence the system. The baseline conditions for the analysis are a gas temperature (T_g) of 300 °C and a gas velocity (U_g) of approximately 3.15 m/s. The following parameters was varied:

1. Gas temperature (T_g), altered by ±10% to evaluate its effect on heat transfer to the bed.
2. Gas velocity (U_g) along the vertical position in the bed.
3. Particle diameter, increased by 10% to 13.255 mm in one case and decreased by 10% to 10.845 mm in another. This adjustment also required recalculation of the Darcy–Forchheimer coefficients.
4. Changes in pellet composition, leading to variations in heat capacity. For the sensitivity analysis, hematite content is varied between 80% (lower limit), 90% (central case) and 100% (upper limit), with the remainder made up of dolomite — a common additive — to assess the impact of mineralogical composition on thermal properties.
5. Alterations in bed porosity, which, similar to the changes in particle diameter, required a recalculation of the Darcy-Forchheimer coefficients.
6. Constant and temperature dependent (C_p)

The results of this sensitivity analysis will help identify which parameters have the most significant impact on heat transfer.

2.4. Numerical accuracy

Numerical solutions always exhibit various types of errors, primarily including modeling errors, iteration errors and discretization errors [31]. Iteration errors are primarily controlled by setting a convergence criterion for the iterative equation solver to reach an initial residual tolerance of 1×10^{-5} for all calculated field variables before proceeding to the next time step. Modeling errors are more challenging to quantify, but validation against experiments provides a good indication of the model's accuracy. Discretization errors will be addressed in the following subsection.

Mesh sensitivity was evaluated using the Richardson extrapolation method with three successively refined meshes (refinement ratio $r = 2$). The computed order of convergence was $p = 0.938$, with estimated errors below 1% and a grid convergence index (GCI) under 0.02%. A mesh with 200 cells was chosen based on convergence behavior and computational cost. The solution variable is plotted in Fig. 4 together with the extrapolated solution predicted by Richardson's extrapolation Eq. (B.2). Full details of the analysis are provided in Appendix B.

3. Results and discussion

The results of the heat transfer simulations are compared to experimental data for three different isothermal gas temperatures: 300 °C (Fig. 5(a)), 500 °C (Fig. 5(b)), and 700 °C (Fig. 5(c)).

The comparison reveals that the Rowe and the Wakao models produce the most accurate results, both in numerical values and in the shape of the curves. The Wakao model produces values so close to those of the Rowe model that the difference is nearly indistinguishable in the figures. Since the Wakao model assumes a porosity of approximately 0.4, the Rowe model appears to be a better choice if the bed porosity differs significantly from this value.

The Gunn, Tavassoli, and Gnielinski models also perform nearly as well as the Rowe and Wakao models. The modified Ranz–Marshall model (Eq. 6) accounts for porosity but is fundamentally based on a correlation developed for a single, isolated sphere. Simply scaling the original relation to include porosity may not adequately capture the complex heat transfer mechanisms in a packed bed. This is reflected in the results, where the model's curve shows a greater deviation from experimental data compared to the other models.

At higher temperatures, the predicted temperatures for the bottom layers deviate more from the experimental data. It is also observed that the measured bed temperatures in the bottom layers do not reach the gas temperatures of 500 °C or 700 °C. Measured data from the roster also confirms a lower temperature in this region. A plausible explanation for this could be heat losses through conduction or radiation from the roster, resulting in a temperature gradient within the bed. This gradient may facilitate particle–particle conductive heat flow through the bed. Additional factors that may contribute to the deviations include experimental uncertainties, such as variations in porosity near the walls and at the bed boundaries, localized gas temperature gradients leading to hotspots, and misalignments between thermocouple positions.

3.1. Sensitivity analysis

1. The sensitivity analysis for changes in gas temperature is shown in Fig. 6(a), illustrating that the bed reaches end temperatures of 330 °C when the gas temperature is increased and 270 °C when the gas temperature is decreased. The temperature profiles remain smooth, and in all cases, the bed temperature approaches the gas temperature, which confirms the reliability of the simulations as the results align with physical expectations.
2. The sensitivity analysis for gas velocity, shown in Fig. 6(b), reveals that even small changes in velocity can lead to significant variations in particle temperatures, particularly in the lower parts of the bed, where deviations between simulation and experiment are more pronounced. Furthermore, the figure demonstrates that a small decrease in velocity of 10% significantly improves the fit for the Rowe–Claxton model.
   The velocity was initially estimated from mass flow rates to the burner and later refined within the pellet bed using the momentum equation and the Darcy–Forchheimer approximation. However, this multi-step estimation process introduces an additional source of uncertainty in the resulting velocity field.

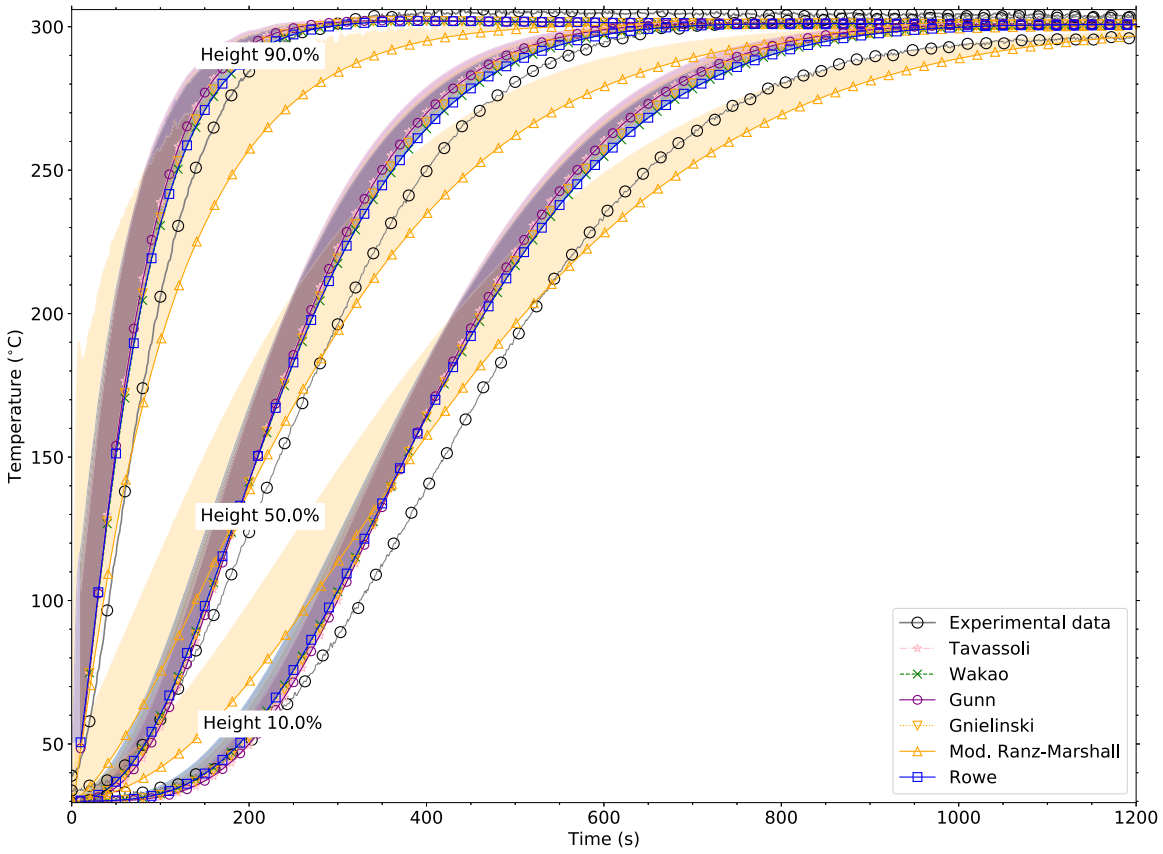

(a) The bed is heated by a downdraft flow of isothermal gas at 300 °C.

Fig. 5. Comparison of particle temperature profiles using various convective heat transfer Nusselt number correlations with experimental data at different bed heights. The difference between the gas temperature and the particle temperature is also plotted as a slightly transparent fill-between region.

3. The influence of particle (or iron ore pellet) diameter is explored in Fig. 6(c). Smaller particles lead to a slightly increased rate of heat transfer, resulting in steeper temperature profiles in the simulation.
4. A change in particle composition yields only minor effects on heat transfer as shown in Fig. 6(d). Assuming the particles are composed entirely of hematite appears reasonable in this scenario.
5. The effect of varying bed porosity is shown in Fig. 6(e). A higher porosity reduces the rate of heat transfer, while a lower porosity increases it, with the most pronounced differences occurring in the lower layers of the packed bed.
6. Finally, including a temperature-dependent heat capacity significantly improves the agreement between simulations and experimental data when using the Rowe–Claxton heat transfer model, as shown in Fig. 6(f).

Although the pressure drop models do not precisely predict experimental values, the sensitivity analysis indicates that accurately simulating the velocity field is crucial; otherwise, there can be substantial deviations between simulated and experimental bed temperatures.

The results from the validation of the Darcy–Forchheimer parameters are presented in Table 7, alongside the measured values. These experimental results are crucial in understanding the gas velocity behavior within the porous bed. The pressure drop experiment conducted at 300 °C and a gas velocity of $3.15\,\mathrm{m\,s^{-1}}$, results in somewhat higher pressure drop then in the real scenario, suggesting that a slight reduction in the velocity field may enhance the fit of heat transfer simulations to experimental data.

Table 7
Pressure drop experiments used for validating the Darcy–Forchheimer parameters.

Velocity $\mathbf{U}$ ($\mathrm{m\,s^{-1}}$)	Gas temp T_g (°C)	Measured Δp (kPa)	Simulated Δp (kPa)	Mass flow $\dot{m}$ ($\mathrm{kg\,h^{-1}}$)	Re_p [a,b]
3.15	300	4.5	4.73	700	820
4.2	500	6.25	6.51	700	660
5.2	700	8.1	8.59	700	590

[a] Typical gas properties were $\mu = 2.7 \times 10^{-5}, 3.3 \times 10^{-5}$ and $3.8 \times 10^{-5}\mathrm{kg/(m\,s)}$, and $\rho = 0.58, 0.43$ and $0.36\,\mathrm{kg/m^3}$ at 300 °C, 500 °C and 700 °C, respectively.
[b] Calculated as $Re_p = \frac{\rho \mathbf{U} d_p}{\mu}$.

4. Conclusions

This study evaluated various heat transfer models for a packed bed system and compared their predictions to experimental data at different gas temperatures. The results indicate that the Rowe–Claxton and Wakao–Funazkri models provide the most accurate predictions, both in numerical values and curve shapes. Given that the Wakao–Funazkri model assumes a porosity of approximately 0.4, the Rowe–Claxton model may be a more suitable choice when bed porosity deviates significantly from this value.

The Rowe–Claxton model showed better agreement with experimental data than the modified Ranz–Marshall model, highlighting the importance of isolating convective heat transfer from overlapping thermo-chemical effects. This emphasizes the need for experiments under stable and well-defined conditions, such as isothermal gas environments, to reduce transient influences. Clear documentation of

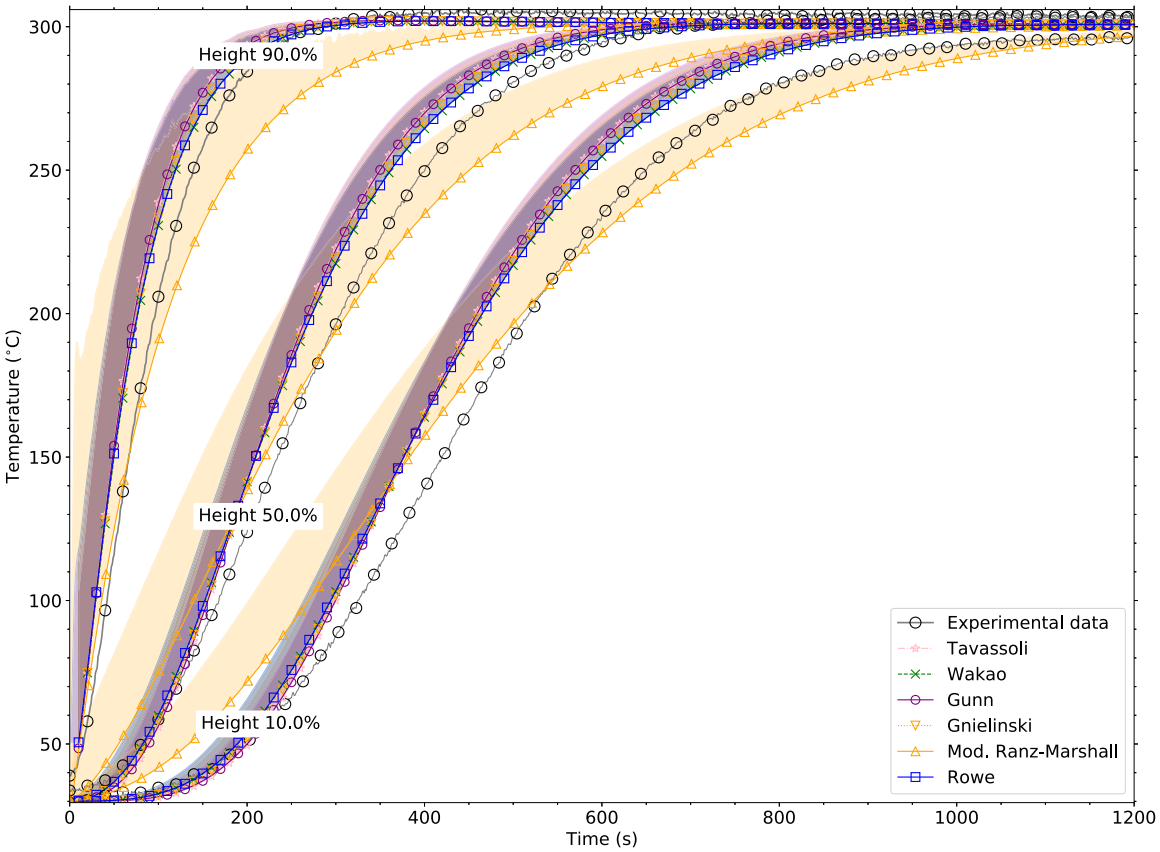

(b) The bed is heated by a downdraft flow of isothermal gas at 500 °C.

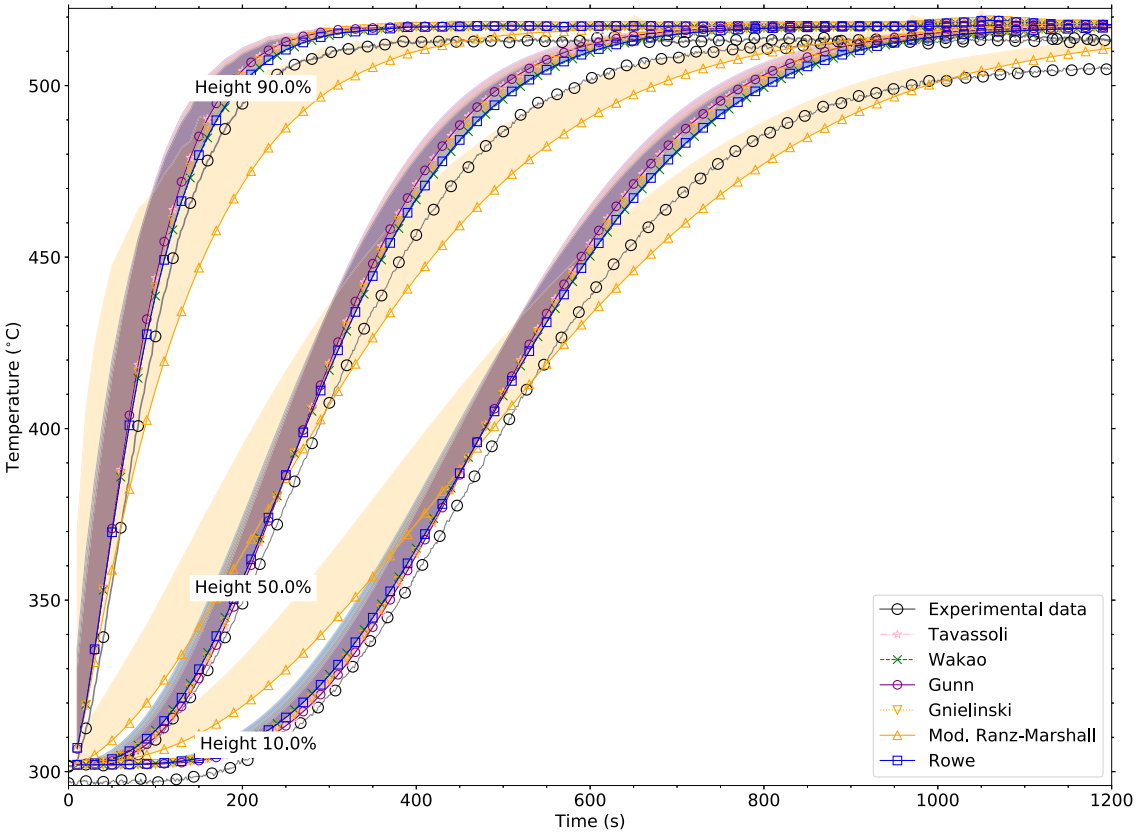

(c) The bed is heated by a downdraft flow of isothermal gas at 700 °C.

Fig. 5. (*continued*).

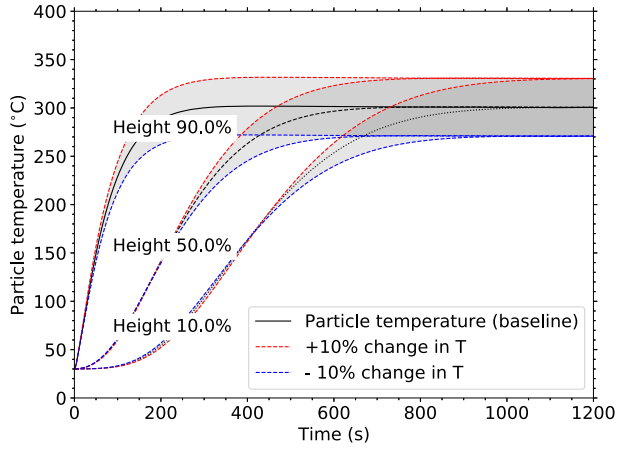

(a) Sensitivity analysis with a 10% change in gas temperature.

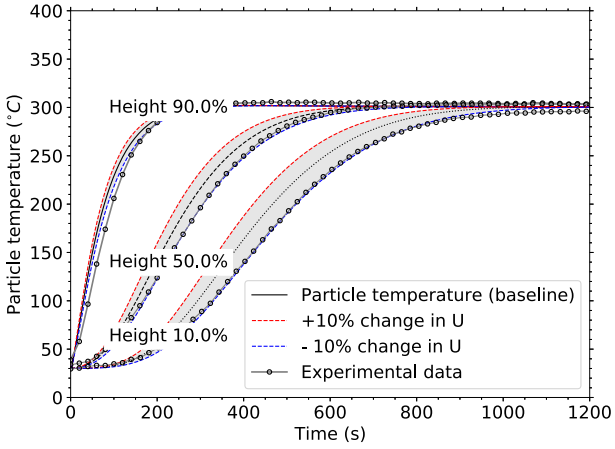

(b) Sensitivity analysis with a 10% change in the gas velocity.

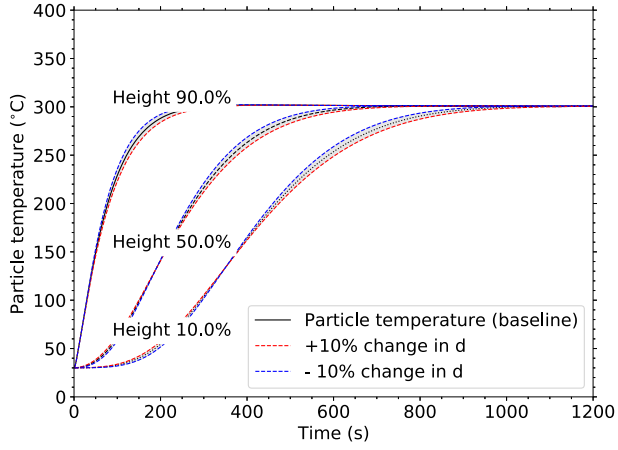

(c) Sensitivity analysis with a 10% change in pellet diameter.

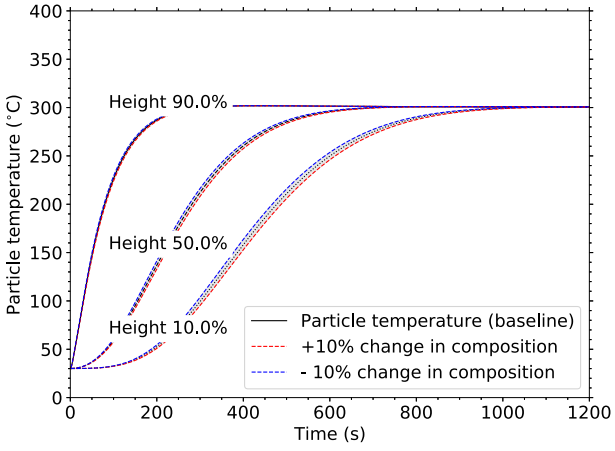

(d) Sensitivity analysis with 100%, 90% (baseline) and 80% hematite content in pellet composition.

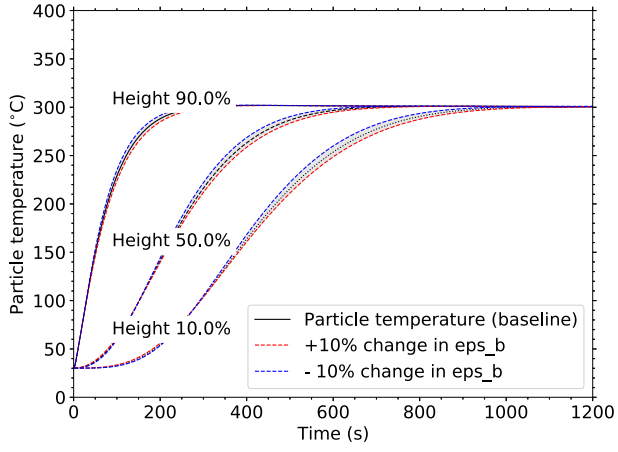

(e) Sensitivity analysis with a 10% change in bed porosity.

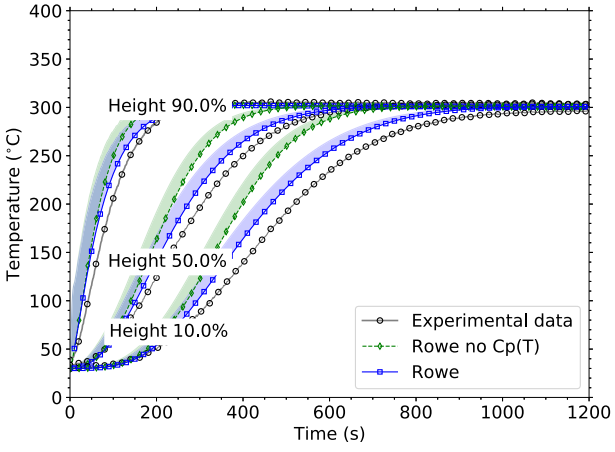

(f) Sensitivity analysis with and without temperature-dependent heat capacity.

Fig. 6. Sensitivity analysis for temperature, pellet diameter, pellet composition, bed porosity and heat capacity. The plots shows the pellet temperature in the upper, bottom and the middle layer of the bed.

modeling assumptions, such as the use of temperature-dependent heat capacity models, also plays a key role in ensuring reproducibility and enabling meaningful comparison across studies.

Another key finding is the strong influence of gas velocity on heat transfer. A modest 10% reduction in gas velocity significantly improves agreement between simulated and measured bed temperatures.

At higher gas temperatures, the measured particle temperatures in the lower bed layers did not fully approach the gas temperature. This indicates that additional heat transfer mechanisms or boundary effects may influence the system. Future work should investigate these effects more systematically, including potential conductive heat losses to the grate, radiation, and the influence of local porosity variations. Improved gas velocity estimation and extended diagnostics are expected to further enhance model accuracy.

CRediT authorship contribution statement

Örjan Fjällborg: Writing – original draft, Visualization, Validation, Software, Methodology, Investigation, Conceptualization. **Charlotte Andersson:** Writing – review & editing, Supervision. **Daniel Marjavaara:** Writing – review & editing, Supervision. **T.K. Sandeep Kumar:** Writing – review & editing, Supervision. **Anders Dahlin:** Writing – review & editing, Data curation.

Declaration of Generative AI and AI-assisted technologies in the writing process

During the preparation of this work, the author(s) used ChatGPT (OpenAI) to assist in improving clarity, grammar, and phrasing. After using this tool, the author(s) reviewed and edited the content as needed and take(s) full responsibility for the content of the publication.

Declaration of competing interest

The authors declare that they have no known competing financial interests or personal relationships that could have appeared to influence the work reported in this paper.

Acknowledgments

This project was partially funded by Swedish Mining Innovation, a joint initiative between Formas, Vinnova and the Swedish Energy Agency.

Appendix A. Derivation of porous media model and coefficients

It is common to use CFD with a porous zone to model fluid flow through porous media [32,33]. This approach often approximates the behavior of the porous zone using the Darcy–Forchheimer equation, which combines Darcy's law for viscous drag with an additional inertial term to account for higher velocities and turbulence. This method offers a significant reduction in computational cost compared to CFD-DEM simulations, which track individual particles and their interactions. While the Darcy–Forchheimer model provides good overall accuracy, particularly for predicting pressure drops and average flow behavior, it may not capture specific local flow conditions within the porous medium. Therefore, it is a suitable choice when detailed microscale flow analysis is not required. In Eq. (9), the term S_m is given by the Darcy–Forchheimer law

$$S_\mathrm{m} = \left(\mu\mathbf{D} + \frac{1}{2}\rho\mathbf{F}\mathbf{U}\right)\mathbf{U}, \tag{A.1}$$

where $\mathbf{D}$ is the Darcy coefficient and $\mathbf{F}$ is the Forchheimer coefficient. S_m can also be seen as a pressure gradient ∇p. The pressure drop Δp over a bed of length L with the superficial velocity U_sv can be expressed by the Ergun equation [34] as

$$\Delta p = \frac{150\mu L}{d_\mathrm{p}^2}\frac{\left(1-\epsilon_\mathrm{b}\right)^2}{\epsilon_\mathrm{b}^3}U_\mathrm{sv} + \frac{1.75L\rho}{d_\mathrm{p}}\frac{\left(1-\epsilon_\mathrm{b}\right)}{\epsilon_\mathrm{b}^3}U_\mathrm{sv}|U_\mathrm{sv}|. \tag{A.2}$$

The superficial velocity is connected to the physical velocity by

$$U_\mathrm{sv} = U\cdot\epsilon_\mathrm{b} \tag{A.3}$$

Table B.8
Mesh independence study solution variables.

	Cells	Value (°C)
ϕ_3 (coarse)	25	256.53
ϕ_2 (medium)	50	260.884
ϕ_1 (fine)	100	263.157

Table B.9
Error estimation in mesh independence study.

	Cells	Error (%)
ξ_3 (coarse)	25	3.429
ξ_2 (medium)	50	1.79
ξ_1 (fine)	100	0.935

And converting Eq. (A.2) into a pressure drop (or a pressure gradient over the whole bed), by dividing Eq. (A.2) by L gives

$$\frac{\Delta p}{L} = \nabla p = \frac{150\mu}{d_\mathrm{p}^2}\frac{\left(1-\epsilon_\mathrm{b}\right)^2}{\epsilon_\mathrm{b}^3}U_\mathrm{sv} + \frac{1.75\rho}{d_\mathrm{p}}\frac{\left(1-\epsilon_\mathrm{b}\right)}{\epsilon_\mathrm{b}^3}U_\mathrm{sv}|U_\mathrm{sv}|. \tag{A.4}$$

Noticing that the Ergun equation is now on the same form as the Darcy–Forchheimer law, the Darcy and the Forchheimer coefficients can be extracted from the Ergun equation as

$$D = \frac{150}{d_\mathrm{p}^2}\frac{\left(1-\epsilon_\mathrm{b}\right)^2}{\epsilon_\mathrm{b}^3}, \tag{A.5}$$

$$F = 2\cdot\frac{1.75}{d_\mathrm{p}}\frac{\left(1-\epsilon_\mathrm{b}\right)}{\epsilon_\mathrm{b}^3}. \tag{A.6}$$

Appendix B. Mesh independence study

A grid convergence analysis was performed by means of the Richardson extrapolation method [35,36] with three different meshes and a constant refinement ratio r of 2 between the coarse, medium and the fine mesh. The temperature in the middle of the bed at second 400 was selected as the solution variable in the three cases: ϕ_3 (coarse), ϕ_2 (medium), ϕ_1 (fine) and used for calculating the order of convergence given by

$$p = \frac{\ln\left(\frac{\phi_3-\phi_2}{\phi_2-\phi_1}\right)}{\ln(r)}, \tag{B.1}$$

and used to extrapolate the extrapolated solution given by

$$\phi_\mathrm{extrapolated} = \phi_1 - \frac{\phi_2-\phi_1}{r^p-1} \tag{B.2}$$

giving the solution variables in Table B.8 with the error estimations given by

$$\xi_3 = \left|1-\frac{\phi_3}{\phi_\mathrm{extrapolated}}\right| \tag{B.3}$$

$$\xi_2 = \left|1-\frac{\phi_2}{\phi_\mathrm{extrapolated}}\right| \tag{B.4}$$

$$\xi_1 = \left|1-\frac{\phi_1}{\phi_\mathrm{extrapolated}}\right| \tag{B.5}$$

which leads to the estimated errors found in Table B.9 when simulated. Additional simulations were performed with finer meshes containing 200 and 500 cells in the bed area, and the temperature was plotted in Fig. 4 together with the extrapolated solution predicted by Richardson's extrapolation (Eq. (B.2)). As noted in the figure, the temperature converges towards the extrapolated solution as the mesh is refined. However around 200 cells, the rate of convergence significantly decreases. Therefore, this cell count in the bed area is chosen for subsequent simulations, as it gives a reasonably accurate error estimate. Further mesh refinement would result in a substantial increase in

computational time with only a minor reduction in discretization error. The estimated error is even slightly lower than 1% which it already was when using 100 cells. The grid convergence index is given by

$$\mathrm{GCI}_{12} = \frac{1.25}{r^p - 1}\left|\frac{\phi_1 - \phi_2}{\phi_1}\right| \tag{B.6}$$

and

$$\mathrm{GCI}_{23} = \frac{1.25}{r^p - 1}\left|\frac{\phi_2 - \phi_3}{\phi_2}\right| \tag{B.7}$$

giving

$$\mathrm{GCI}_{12} = 0.0118\%$$

$$\mathrm{GCI}_{23} = 0.0228\%$$

and the asymptotic range of convergence given by

$$\mathrm{Conv} = \frac{\mathrm{GCI}_{23}}{r^p \cdot \mathrm{GCI}_{12}} \tag{B.8}$$

resulting in

$$\mathrm{Conv} = 1.008$$

which indicates that the extrapolated solution is grid independent since the asymptotic range of convergence is near the value 1.

Data availability

Data will be made available on request.

References

[1] HYBRIT, A value chain for fossil-free steel, 2024, https://www.hybritdevelopment.com/en/a-value-chain-for-fossil-free-steel. (Accessed 21 May 2025).

[2] Midrex Technologies, Inc., Midrex H_2 – towards CO_2-free direct reduction, 2021, https://www.midrex.com/midrex-process/midrex-h2/. (Accessed 21 May 2025).

[3] Stegra, Our platforms – green hydrogen, iron and steel, 2024, https://stegra.com/green-platforms. (Accessed 21 May 2025).

[4] Salzgitter AG, The concept for a sustainable future, 2024, https://salcos.salzgitter-ag.com/en/salcos.html. (Accessed 21 May 2025).

[5] K1-MET, Susteel – sustainable steel production utilising hydrogen, 2024, https://www.k1-met.com/en/non_comet/susteel/. (Accessed 21 May 2025).

[6] World Steel Association, Breakthrough technologies, 2024, https://worldsteel.org/climate-action/breakthrough-technologies/. (Accessed 21 May 2025).

[7] G. Naterer, Heat Transfer in Single and Multiphase Systems, CRC Press, United States of America, 2003.

[8] F.P. Incropera, D.P. DeWitt, Fundamentals of Heat and Mass Transfer, sixth ed., John Wiley & Sons, 2007.

[9] V. Seshadri, R.O.S. Pereira, Comparison of formulae for determining heat transfer coefficient of packed beds, Trans. ISIJ 26 (1986) 604–610.

[10] M. Barati, Dynamic simulation of pellet induration process in straight-grate system, Int. J. Miner. Process. 89 (2008) 30–39.

[11] J.A. Thurlby, R.J. Batterham, R.E. Turner, Development and validation of a mathematical model for the moving grate induration of iron ore pellets, Int. J. Miner. Process. 6 (1978) 43–64.

[12] J. Thurlby, A dynamic mathematical model of the complete grate/kiln iron-ore pellet induration process, Met. Trans. B 19B (1988) 103–112.

[13] S. Tan, J. Peng, H. Shi, Modeling and simulation of iron ore pellet drying and induration process with accurate bed void fraction calculation, Dry. Technol. 34 (2016) 651–664.

[14] S. Dave, S. Patra, S. Pabat, et al., A mathematical model for straight-grate iron oxide pellet induration furnace: Formulation, plant scale validation, Instrum. Process. Model. Valid. 75 (2023) 2406–2420.

[15] T. Thorat, V. Nurni, M. Basavarja, et al., Modelling of heat transfer in a straight grate pellet induration reactor complemented with plant scale experiments, Miner. Process. Extr. Met. 131 (3) (2022) 283–289.

[16] P.N. Rowe, K.T. Claxton, Heat and mass transfer from a single sphere to fluid flowing through an array, Trans. Inst. Chem. Eng. 43 (1965) T321.

[17] T.F.N. Wakao, S. Kaguei, Effect of fluid dispersion coefficients on particle-to-fluid heat transfer coefficients in packed beds, Chem. Eng. Sci. 34 (1979) 325–336.

[18] D.J. Gunn, Transfer of heat or mass to particles in fixed and fluidised beds, Int. J. Heat Mass Transfer 21 (1978) 467–476.

[19] V. Gnielinski, Formula for calculating the heat and mass transfer in through flow of a fixed bed at medium and large peclet, Process-Technol. 12 (1978) 63–366.

[20] H. Tavassoli, Direct Numerical Simulation of Dense Gas–Solids Non-Isothermal Flows, Eindhoven University of Technology, 2014.

[21] E. Achenbach, Heat and flow characteristics of packed beds, Exp. Therm. Fluid Sci. 10 (1) (1995) 17–27, http://dx.doi.org/10.1016/0894-1777(94)00077-L, URL https://www.sciencedirect.com/science/article/pii/089417779400077L.

[22] A. Eriksson, C. Andersson, P. Semberg, T.K.S. Kumar, A. Dahlin, H. Ahmed, Effects of high-oxygen-level process gas (40 temperature and strength development of a magnetite pellet bed during pot furnace induration, ISIJ Int. 62 (3) (2022) 465–476, http://dx.doi.org/10.2355/isijinternational.ISIJINT-2021-390.

[23] J. Szekely, J.W. Evans, H.Y. Sohn, Gas-Solid Reactions, Academic Press, New York, San Fransico, London, 1976.

[24] H.Y. Sohn, Fluid-Solid Reactions, Elsevier, Amsterdam, Oxford, Cambridge, 2020.

[25] Air properties – density, viscosity, thermal conductivity, heat capacity, etc., 2025, https://www.engineeringtoolbox.com/air-properties-d_1509.html. (Accessed 12 October 2025).

[26] N.S. Sundamurti, V. Rao, Thermal conductivity and diffusivity of iron ore pellet having low porosity, ISIJ Int. 42 (7) (2002) 800–802, measured pellet conductivity over temperature range.

[27] DarcyForchheimer, https://openfoamwiki.net/index.php/DarcyForchheimer/. (Accessed 07 February 2023).

[28] B.D. Wood, X. He, S.V. Apte, Modeling turbulent flows in porous media, Annu. Rev. Fluid Mech. 52 (1) (2020) 171–203, http://dx.doi.org/10.1146/annurev-fluid-010719-060317.

[29] Tips and tricks in OpenFOAM, 2023, http://www.wolfdynamics.com/wiki/tipsandtricks.pdf. (Accessed 15 August 2023).

[30] W. Sutherland, The viscosity of gases and molecular force, Phil. Mag. 5 (1893) 507–531.

[31] M. Casey, T. Wintergerste, European research community on flow, turbulence and combustion, in: ERCOFTAC Best Practice Guidelines: ERCOFTAC Special Interest Group on "Quality and Trust in Industrial CFD", ERCOFTAC, 2000.

[32] G. Hellström, S. Lundström, Flow through porous media at moderate reynolds number, in: Proceedings, 4th International Scientific Colloquium Modelling for Material Processing, 2006, pp. 129–134.

[33] U.M. Costa, et al., Inertial effects on fluid flow through disordered porous media, Phys. Rev. Lett. 82 (1999) 5249–5252.

[34] S. Ergun, Chem. Eng. Prog. 48 (1952) 89–94.

[35] L.F. Richardson, J.A. Gaunt, The deferred approach to the limit, Philos. Trans. R. Soc. Lond. Ser. A, Contain. Pap. A Math. Phys. Charact. 226 (1927) 299–361.

[36] P.J. Roache, Quantification of uncertainty in computational fluid dynamics, Annu. Rev. Fluid. Mech. 29 (1997) 123–160.